A High-Resolution Simulation of Typhoon Rananim (2004) with MM5. Part I: Model Verification, Inner-Core Shear, and Asymmetric Convection

QINGQING LI, YIHONG DUAN, AND HUI YU

Shanghai Typhoon Institute, and Laboratory of Typhoon Forecast Technique/CMA, Shanghai, China

GANG FU

Department of Marine Meteorology, Ocean University of China, Qingdao, China

(Manuscript received 29 January 2007, in final form 23 October 2007)

ABSTRACT

In this study, the fifth-generation Pennsylvania State University–National Center for Atmospheric Research (PSU–NCAR) Mesoscale Model (MM5) is used to simulate Typhoon Rananim (2004) at high resolution (2-km grid size). The simulation agrees well with a variety of observations, especially for intensification, maintenance, landfall, and inner-core structures, including the echo-free eye, the asymmetry in eyewall convection, and the slope of the eyewall during landfall. The asymmetric feature of surface winds is also captured reasonably well by the model, as well as changes in surface winds and pressure near the storm center.

The shear-induced vortex tilt and storm-relative asymmetric winds are examined to investigate how vertical shear affects the asymmetric convection in the inner-core region. The inner-core vertical shear is found to be nonunidirectional, and to induce a nonunidirectional vortex tilt. The distribution of asymmetric convection is, however, inconsistent with the typical downshear-left pattern for a deep-layer shear. Qualitative agreement is found between the divergence pattern and the storm-relative flow, with convergence (divergence) generally associated with asymmetric inflow (outflow) in the eyewall. The collocation of the inflow-induced lower-level convergence in the boundary layer and the lower troposphere and the midlevel divergence causes shallow updrafts in the western and southern parts of the eyewall, while the deep and strong upward motion in the southeastern portion of the eyewall is due to the collocation of the net convergence associated with the strong asymmetric flow in the midtroposphere and the inflow near 400 hPa and its associated divergence in the outflow layer above 400 hPa.

1. Introduction

The forecasting of tropical cyclone (TC) movement has steadily improved over the last three decades largely because of a combination of better observations (Tuleya and Lord 1997; Soden et al. 2001), improved numerical models (DeMaria and Kaplan 1997; Kurihara et al. 1995), and an in-depth understanding of physical processes and mechanisms that control the motion of TCs (George and Gray 1976; Holland 1983, 1984; Chan 1984; Wang et al. 1998; Chan et al. 2002; and others). By contrast, the skill in the prediction of TC structure and intensity changes remains relatively low despite the application of sophisticated numerical models (DeMaria and Kaplan 1997; Wang and Wu 2004). One major reason for this low skill is that the physical processes associated with intensity changes are not well understood (Neumann 1997). Recent studies have suggested that TC structure and intensity changes could be caused by many different physical mechanisms governing the inner-core structure as well as interactions among storm, underlying ocean surface, and large-scale environment (Montgomery and Kallenbach 1997; Chan et al. 2001; Wang 2002a,b; Black et al. 2002; Wang and Wu 2004; Wu et al. 2005).

For this reason, more and more studies have used high-resolution numerical simulations to explore the processes associated with inner-core structures and vortex dynamics. Liu et al. (1997) successfully simulated the inner-core structure of Hurricane Andrew (1992) by employing a nested-grid (54, 18, and 6 km) version of the fifth-generation Pennsylvania State University–

Corresponding author address: Qingqing Li, Shanghai Typhoon Institute, 166 Puxi Road, Shanghai 200030, China.
E-mail: liqq@mail.typhoon.gov.cn

DOI: 10.1175/2007MWR2159.1

National Center for Atmospheric Research (PSU–NCAR) Mesoscale Model (MM5; Dudhia 1993; Grell et al. 1995) and further analyzed its kinematic and thermodynamic structures (Liu et al. 1999). A series of studies have been carried out by Zhang et al. (2000, 2001, 2002) and Yau et al. (2004) to investigate the vertical forcing dynamics in the eye and eyewall, the role of the supergradient flow, the thermodynamic budget of the TC, the genesis of small-scale wind streaks, and the influence of varying surface fluxes on changes in storm inner-core structures and intensity. Frank and Ritchie (2001) examined the structure and intensity changes resulting from the vertical shear in idealized simulations using a 5-km fine mesh. Wang (2002a,b) showed the overall structure of vortex Rossby waves in a simulated TC, analyzed the potential vorticity and eddy kinetic energy budgets, and investigated the role of vortex Rossby waves in TC structure and intensity changes. By using a cloud-resolving simulation, Braun (2002) discussed asymmetric inner-core structures of Hurricane Bob (1991) and analyzed the relationship between buoyancy and eyewall updrafts. Rogers et al. (2003) examined the interaction between the storm and its environmental flow through a high-resolution modeling study of Hurricane Bonnie (1998) and found that the accumulated rainfall was distributed symmetrically across the track of the storm when the vertical shear was strong and across track, but asymmetrically across the track when the shear was weak and along track. Zhu et al. (2004) used a numerical simulation with a fine grid size of 4 km to discuss the evolution of the eyewall of Hurricane Bonnie (1998). Zhu and Zhang (2006) also conducted sensitivity simulations and examined the effects of various cloud microphysics processes on the intensity, precipitation, and inner-core structures.

Observational studies suggested that environmental vertical wind shear has an important impact on the distribution of convection in the inner-core region. In general, the maximum rainfall tends to occur on the left side of the shear vector (in a downshear sense; e.g., Marks et al. 1992; Franklin et al. 1993; Chan et al. 2004). Several mechanisms have recently been proposed to explain how vertical shear causes asymmetric convection in adiabatic vortices.

One mechanism is a balanced response to a slant vortex that leads updrafts to the downtilt direction (Jones 1995; Wang and Holland 1996; Frank and Ritchie 1999). This mechanism is, however, only effective for a short period after the tilting of the adiabatic vortex. Afterward, a second mechanism becomes dominant. The adiabatic interaction of the vortex flow with temperature anomalies triggered by the vortex tilt causes an upward motion 90° to the right of the tilt direction (Jones 1995; Wu and Wang 2001).

The third mechanism is related to the storm-relative asymmetric flow (Willoughby et al. 1984; Bender 1997; Frank and Ritchie 2001). Bender (1997) demonstrated that the direction of the relative asymmetric flow determines where the maximum rainfall occurred. Based on the conservation of vorticity, strong vorticity advection must be first-order balanced by stretching or compressing of the vortex tube, which produces convergence (divergence) where there is inflow (outflow) in the eyewall. Braun et al. (2006) conducted a high-resolution simulation of Hurricane Bonnie (1998) and found that the convective asymmetry was qualitatively consistent with the foregoing balance between vorticity advection by the relative flow and the stretching of the vortex tube, with asymmetric inflow (convergence) at lower levels and outflow (divergence) at upper levels on the downshear side of the eyewall. They also showed that the upward motion portion of the eyewall asymmetry was located in the direction of the vortex tilt, consistent with the vertical motion required to maintain dynamic balance. A similar relationship was also found in the high-resolution numerical modeling of Hurricane Erin (2001) by Wu et al. (2006).

It should be pointed out that the wind shear in these simulations was usually unidirectional (e.g., Fig. 3 in Frank and Ritchie 2001) or approximately unidirectional in the vertical, and focused only on the shear between the lower and upper layers, not the shear in the midtroposphere. The features of vortex tilt and asymmetric convection with respect to nonunidirectional and complex vertical shear remain unclear and should therefore be investigated further.

In the current study, we will reproduce the evolution of Typhoon Rananim (2004) with a high-resolution model and investigate the features of inner-core vertical wind shear and vortex tilt, and their mutual effects on the inner-core asymmetric convection. The rest of the paper is organized as follows. Section 2 gives a brief overview of Typhoon Rananim and describes the model configuration. Section 3 presents a detailed verification against various available observations. Section 4 describes the simulated inner-core vertical shear, vortex tilt, and asymmetric convection. The main conclusions are given in section 5.

2. Case overview and model description

a. Overview of Typhoon Rananim (2004)

Typhoon Rananim can be traced back to a tropical disturbance with organized deep convection about

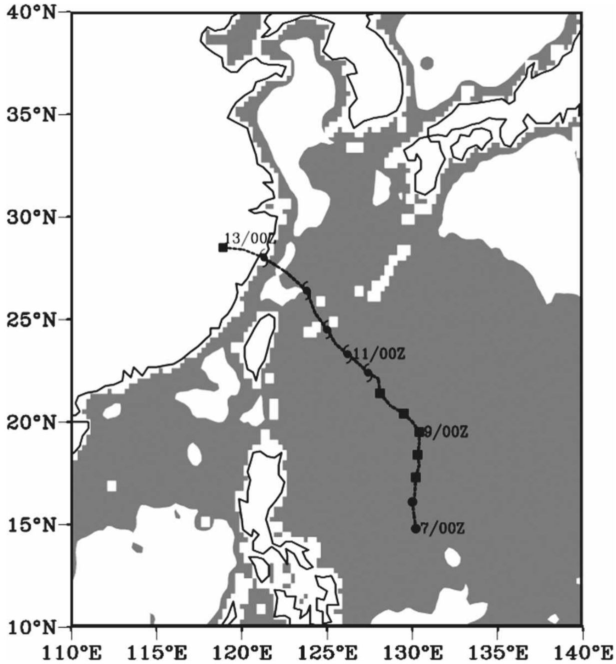

FIG. 1. The best track of Rananim derived from the JTWC is presented and the best-track intensities for typhoon (typhoon symbol), tropical storm (box), and tropical depression (dot) are indicated. Symbols are drawn at 12-h intervals. Areas with the SST > 29°C derived from the optimally interpolated microwave SST products are shaded.

1000 km east of Manila in the Philippines, over warm water with the sea surface temperature (SST) > 29°C (Fig. 1). It was categorized as a tropical depression by the Joint Typhoon Warning Center (JTWC) at 0000 UTC 7 August. At 0000 UTC 8 August, the system strengthened into Tropical Storm Rananim with its minimum sea level pressure (MSLP) falling to 997 hPa. It headed northward slowly along the northwestern periphery of a near-equatorial ridge. The storm turned northwestward at 0000 UTC 9 August. The maximum surface wind (MSW) increased during the day from about 25 m s^{-1} at 0000 UTC 9 August to 30 m s^{-1} at 1800 UTC 9 August. Rananim was upgraded to a typhoon at 1200 UTC 10 August, with the MSW reaching approximately 35 m s^{-1}. Rananim continued to intensify and track northwestward, reaching a MSLP of 963 hPa by 0000 UTC 11 August. Its strengthening phase brought the MSW up to 40 m s^{-1}. The storm maintained its peak intensity for about 18 h before beginning to weaken. At 0600 UTC 12 August, Rananim's track shifted to the west-northwest (Fig. 1). It made landfall at approximately 1300 UTC 12 August in China. By 0000 UTC 13 August, Rananim had weakened into a tropical storm. Further weakening occurred as the storm progressed farther west into China.

b. Model description

A 72-h simulation of Typhoon Rananim initialized at 0000 UTC 10 August is conducted using the MM5. Four two-way interactive domains are employed with grid sizes of 54, 18, 6, and 2 km and with domain sizes of 91 × 91, 160 × 160, 268 × 268, and 355 × 355 grid points (see Fig. 2 for the design), respectively. The top of the model is at 50 hPa, and the model has 27 σ levels (0.998, 0.985, 0.970, 0.955, 0.945, 0.890, 0.860, 0.825, 0.775, 0.725, 0.675, 0.625, 0.575, 0.525, 0.475, 0.425, 0.365, 0.325, 0.275, 0.225, 0. 190, 0.160, 0.130, 0.095, 0.050, and 0.025) in the vertical. Both the 54- and 18-km grid domains are integrated for 72 h. To reduce computational cost, the 6- and 2-km domains are activated after 30 and 36 h into the integration, respectively. Although the 2-km mesh is stationary, it can cover the inner-core region of Rananim during the period of interest. The 2-km simulation was repeated for the period between 51 and 57 h (0300–0900 UTC 12 August) with the model output every 5 min to resolve the evolution of inner-core dynamic and thermodynamic structures during the mature stage.

The choice of model physics is critical to simulate TCs realistically (Liu et al. 1997; Braun and Tao 2000, Davis and Bosart 2001; Zhu et al. 2004). The coarse resolution in both the outermost 54-km and the intermediate 18-km domains necessitates the inclusion of cumulus parameterization. After several tests of various cumulus parameterization schemes, the Betts–Miller scheme (Betts and Miller 1986) was found to produce the best simulation. Such a scheme has also been employed by Liu et al. (1997) and Zhang et al. (2005) to simulate other TCs. Although no deep convective parameterization is used in the 6-km grid, a shallow convective scheme in MM5 is still used. Other schemes of physical parameterizations include the Blackadar planetary boundary layer scheme (Zhang and Anthes 1982), mixed-phase cloud microphysics scheme of Reisner and Bruintjes (1998), and cloud radiation scheme of Dudhia (1989).

The initial time of the model is 12 h before Rananim intensified to a typhoon. The run is terminated at 0000 UTC 13 August when the storm moved farther inland and weakened into a tropical storm. The 72-h simulation covers several important stages in the life cycle of Typhoon Rananim, including its steady intensification, its mature stage, and landfall. The initial and lateral boundary conditions are obtained from a 6-hourly global analysis of the National Centers for Environmental Prediction (NCEP) with horizontal resolution of 1° × 1°. The SST data are derived from the NCEP SST analysis.

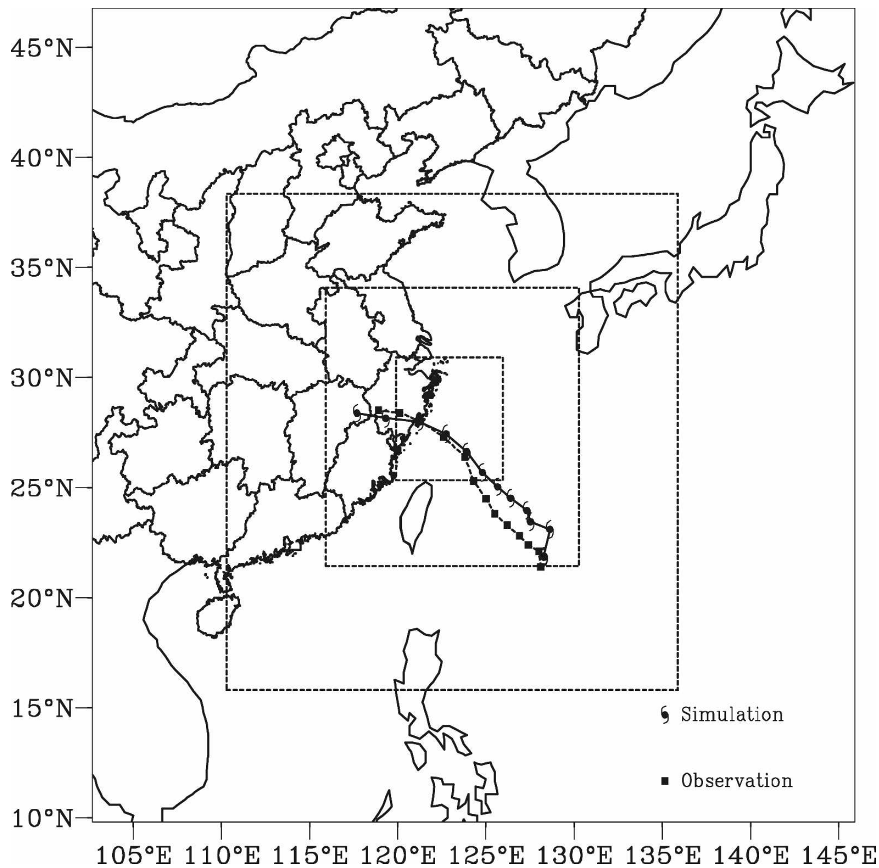

FIG. 2. Design of the model domains with 6-hourly tracks of Typhoon Rananim from the best track (solid boxes) and model simulation (typhoon symbols).

The initial analysis fails to capture the correct intensity of the tropical storm (985-hPa MSLP reported by JTWC, but only 995 hPa in the analysis). To improve the initial vortex structure and intensity, we replace the initial vortex following Liu et al.'s (1997) approach. First, the outermost domain is initialized at 0000 UTC 10 August and run with full model physics for 24 h until the model-produced vortex reaches its MSLP similar to the best-track analysis at the model initial time. The preexisting weak vortex in the initial analysis fields is then removed from the analysis and replaced by the model-generated vortex, which is extracted from the 54-km domain run and merged into the analysis. For the finer-mesh domains, the initial conditions are obtained by interpolating fields from their respective mother domains.

3. Model verification

a. Track and intensity

Compared with the best track derived from JTWC, the simulated cyclone takes a more northward path during the first 6 h (Fig. 2). Then the modeled storm moves west-northwestward and approaches the best track gradually after the first 12 h of simulation (Fig. 2). Because the simulated large-scale flow agrees reasonably well with the observed, the modeled storm heads nearly along the best track of Rananim. Thus, the bias in track prediction decreases to nearly null at 48 h until landfall. The model accurately reproduces the time and location of landfall, with an error of less than 10 km. After its landfall, the modeled storm translates a little southward and tends to be faster than the observation in the last 12 h when it moves inland. This discrepancy is believed to result from a relatively stronger environmental steering current[1] of ~9 m s^{-1} from the modeled

[1] The steering current is computed as follows. First, filter out the storm circulation using the methods of Kurihura et al. (1993, 1995) and Kwon et al. (2002) and compute the averaged currents at each level by averaging over a 100–800-km radial band centered on the TC. Second, compute the layer mean value of the above currents with pressure weight as the value of the steering current associated with the TC.

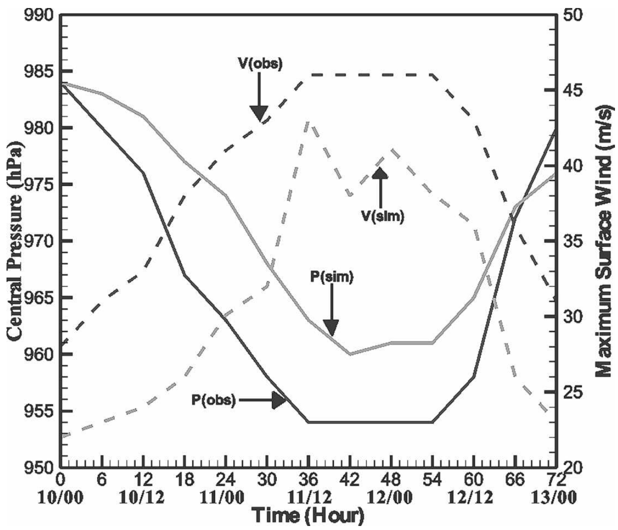

FIG. 3. Time series of the minimum central pressures P (hPa) and maximum surface winds V (m s^{-1}) of Typhoon Rananim from the 72-h simulation [P(sim) and V(sim), respectively] and corresponding best analysis [P(obs) and V(obs), respectively]. Dates and times are provided along the horizontal axis along with model hour and denoted in the form day (dd)/time (hh, UTC).

large-scale flow than the observed one of ~6 m s^{-1}. Despite these discrepancies, the path of the simulated typhoon agrees reasonably well with the observation, especially the landfalling location and time.

A comparison of the MSWs and MSLP between the simulation and best track shows that the simulated intensity is a little weaker than that observed in the deepening stage, with the simulated MSLP reaching 960 hPa, 6 hPa higher than the observation (Fig. 3); however, the intensity trend is well simulated. In particular, both the observation and model show a steady deepening of approximately 1 hPa h^{-1} during the 12-h period after the first 24 h of simulation. The simulated storm achieves its peak intensity at 42 h, about 6 h later than that observed. Then, the simulated storm maintains its peak intensity with a slight weakening (of ~1 hPa) for 12 h. Both the simulated and observed storms begin to weaken at 54 h, which indicates a successful simulation of its landfall of Rananim (see Fig. 2). The observed MSLP rises by 26 hPa while the modeled MSLP rises by 14 hPa in the last 18 h of the integration. During the whole integration, the simulated MSWs are weaker than the corresponding observation, but with the correct trend.

To verify the simulation of intensity change of Rananim when it makes landfall, the surface observations and model outputs at Dachen Island are compared in Fig. 4. (The island is very close to the landfall location, as shown by the filled square in Fig. 6b.) Both the observation and the simulation show increasing winds and decreasing pressure as the storm approaches. The observed peak wind reaches 35 m s^{-1} and the model simulated a peak wind of 29 m s^{-1}. When the eye region passes, the observed wind drops sharply to 3 m s^{-1} while the modeled wind falls to 11 m s^{-1}, with the observed and simulated sea surface pressures decreasing to 968 and 964 hPa, respectively. As the typhoon moves away, pressure significantly increases in both the observation and the simulation. However, it is noticed that the observed wind does not return to the prelandfall value and exhibits fluctuations, which probably implies the effect of mesoscale eddies or roll vortices in the boundary layer (Ian et al. 2005). The simulated storm, however, has surface winds as strong as those at the prelandfall stage. As the model simulates the landfall location accurately, the variation in surface wind direction agrees well with the observations in Dachen Island.

b. Wind and convective structure

As Rananim reaches its mature stage, its surface winds from the National Aeronautics and Space Administration (NASA) Quick Scatterometer (QuikSCAT) data are characterized by an asymmetric structure, with weak winds to the southwest of the center reaching only ~20 m s^{-1} versus >30 m s^{-1} in other directions (Fig. 5a). The model also produces a slight asymmetry (Fig. 5b) with relatively weak winds to the west of the eye. However, it should be noted that strong winds (e.g., >30 m s^{-1}) in the simulation are concentrated near the eyewall region, while in the QuikSCAT data such strong winds are spread outward over a large area, especially in the northwest and southeast quadrants. Interestingly, the simulated weak lee winds east of Taiwan are in good agreement with those observed. Both the simulated and the observed winds present fairly asymmetric distribution of surface winds when the storm is about to make landfall (Figs. 5c and 5d, respectively), like those of many other landfalling TCs (Powell and Houston 1998), with local wind maxima on the northeastern and eastern sides of the eyewall. The modeled surface winds over land are much weaker than those over sea, but stronger than the observations from surface weather stations. In summary, the model can capture fairly well the asymmetric distribution of the surface winds, especially near landfall.

At 1000 UTC 12 August, the observed radar reflectivity shows that the typhoon center is located near 100 km east of Wenzhou (Fig. 6a). Because of the strong convergence forced by the large friction over land, animations of reflectivity show that intense convection in the inner core developed in the northwest quadrant with a weak-echo eye. The model basically reproduces

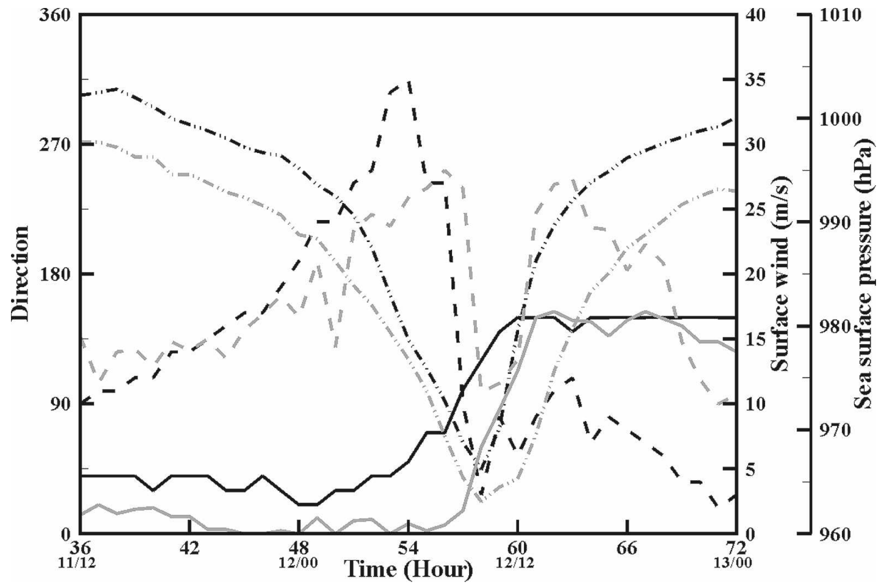

FIG. 4. Black lines show the time series of the sea surface pressure (dot–dashed line; hPa), surface wind (dashed line; m s^{-1}), and surface wind direction (solid lines) at Dachen Island (its location is shown in Fig. 6b). Gray lines denote the simulated results in the same location.

this feature, but with heavier and more extensive precipitation to the northwest and a much bigger eye with a radius of ~100 km (Fig. 6b) compared with ~20 km in the radar data. The observed secondary precipitation maxima occur to the northeast of the eyewall extending to the southeast with several spiral heavy-precipitation bands (Fig. 6a). The simulated secondary precipitation maxima are located in the eastern and southern portion of the eyewall, with more intense convection in those areas (Fig. 6b), indicating a wavenumber-2 asymmetry in convection. The observed weak-echo areas existing in the southwestern quadrant are also simulated qualitatively by the model. About 2 h later, an eyewall is still distinctly defined (Fig. 6c) and three inner rainbands are embedded radially in the east quadrant in the radar imagery, but the model only resolves two rainbands and the eyewall seems to be vaguely defined. The weak-echo area is located along the coast at this time (Fig. 6c). The simulated result appears to portray that feature, although some heavy precipitation is present there (Fig. 6d).

A vertical cross section of the observed reflectivity along the direction of motion of the TC (the arrow in Fig. 6a), approximately from southeast to northwest, shows that the southeastern eyewall is nearly upright (Fig. 7a), and the northwestern part tilts outward with height, which is depicted well in the simulated reflectivity (Fig. 7b). There is a broad rainband (30–70 km) with heavy precipitation adjacent to the eyewall on the southeastern side and another similar structure can be observed farther outward (>70 km). Wide areas of stratiform rain spread over 12 km in the vertical (Fig. 7a). The modeled reflectivity shows several rainbands with multiple embedded cells on the southeastern side (Fig. 7b). Compared with the observation, the simulated eyewall convection is more intense on this side and extends higher in vertical. On the northwestern side, a wide rainband with intense precipitation exists, and strong convection (from ~45 to ~80 km) with reflectivity more than 40 dBZ extends up to around 5-km height (Fig. 7b). Compared with that on the southeastern side, the precipitation on the northwestern side extends up to 9–10 km, lower than the southeastern side. Such a precipitation feature is also captured by the simulation, but with cellular intense convection embedded within it (Fig. 7b).

One hour later, the convection on both sides of the eyewall becomes more intense (Fig. 7c). The model fails to mimic the convective intensification in the eyewall on the southeastern side, but reproduces the wide stratiform precipitation in the upper troposphere. In Fig. 7c, the observed convection in the northwestern portion becomes stronger with the reflectivity more than 40 dBZ extending radially from ~25 to ~75 km. The MM5 seems not to predict the intensification of the eyewall convection on this side, just showing the developing of the multiple convective cells residing in the eye (Fig. 7d).

According to the above verification, the largest difference between the observation and model result is

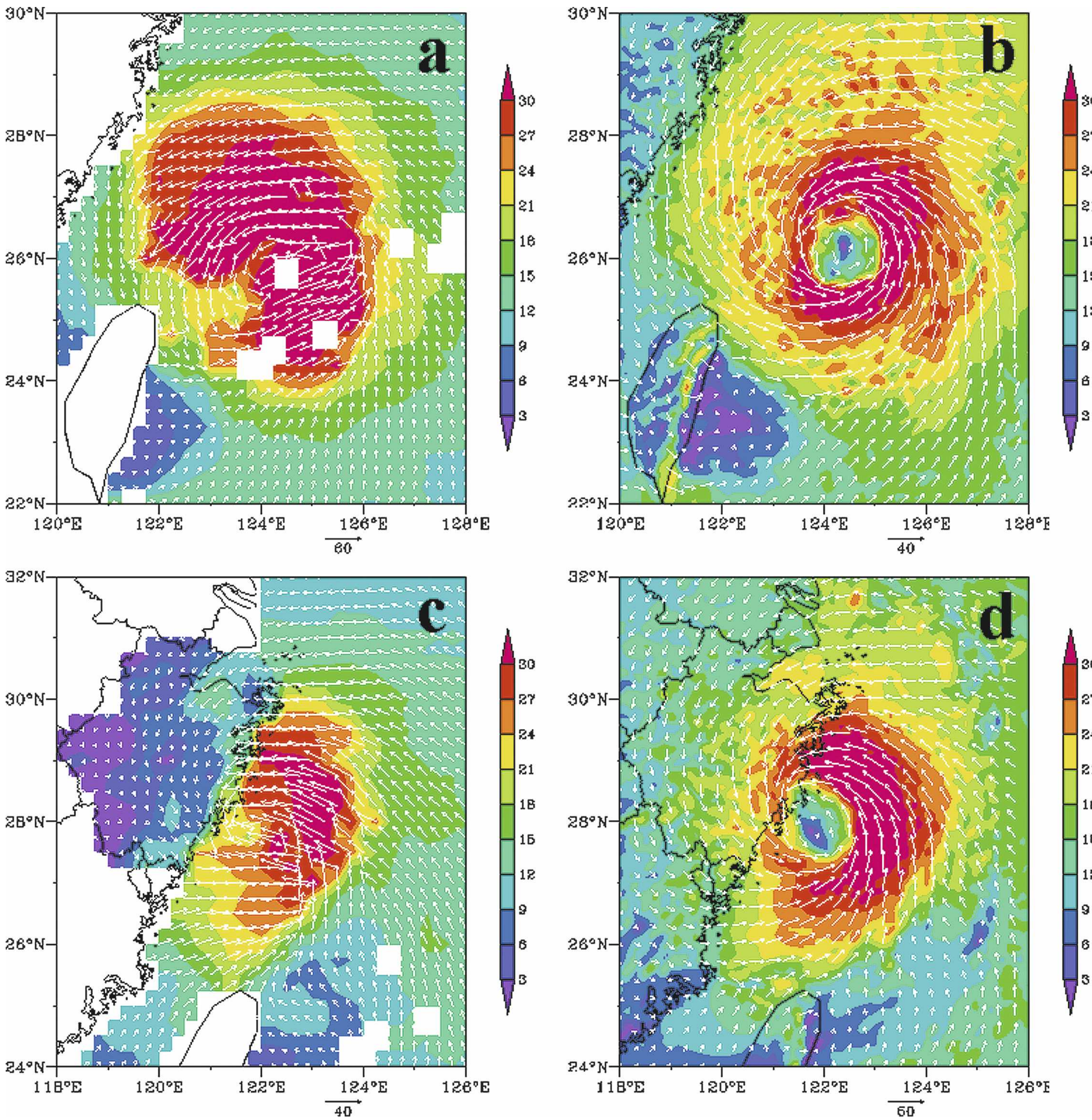

FIG. 5. Comparison of (a) the surface winds derived from QuikSCAT at 2121 UTC 11 Aug with (b) simulated winds at the lowest level at 2100 UTC 11 Aug. (c), (d) As in (a) and (b), respectively, but at 1000 UTC 12 Aug. Note that the surface winds in (c) are the merged products of QuikSCAT and observations of automated surface stations at 1000 UTC 12 Aug. Shading indicates horizontal wind velocity (m s^{-1}), and arrows denote wind vectors.

that MM5 produces an excessively large eye associated with Rananim, which may result from the influence of the relatively large model-generated vortex emerged into the initial fields (Zhang et al. 2005). Wong and Chan (2004) mentioned that TC size can impact on the dynamics of the storm and its interaction with the shear, and thus intensity change. In the Rananim modeling, the model produces a large-size storm with a large eye so that there are some discrepancies in the wind distributions and convective features between the observations and simulation results. Nevertheless, the modeled intensity change and maximum intensity are close to the observations. In addition, these discrepancies do not impede our analyzing and describing the basic processes and general structures observed in Rananim as well as in other storms in the next section.

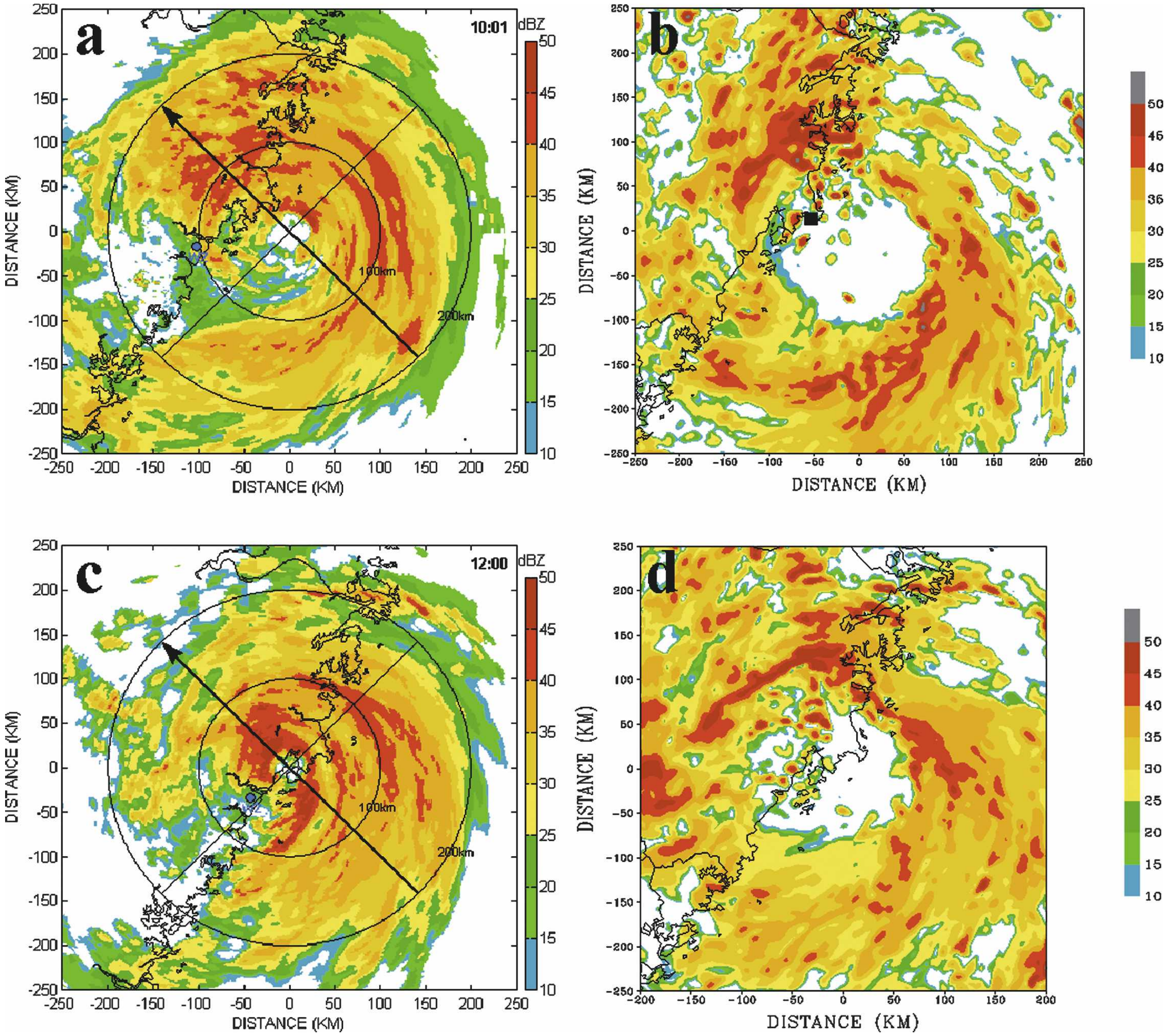

FIG. 6. Two-km-height radar imagery in Wenzhou (blue dot), at (a) 1001 UTC and (c) 1200 UTC 12 Aug along with the storm moving direction (arrows). (b), (d) The 2-km-height simulated reflectivity (dBZ) in the 2-km model at 1000 and 1200 UTC 12 Aug, respectively. The black square in (b) indicates the location of Dachen Island.

4. Inner-core vertical shear, vortex tilt, and convective asymmetry

To examine the inner-core vertical shear, shear-induced vortex tilt, and inner-core convective asymmetry, the model results at 5-min intervals are analyzed from 0300–0900 UTC 12 August. In the current study, the vortex center is defined as the location with the maximum symmetric tangential wind (Wu et al. 2006). The 400-hPa level is defined as the top of layer to discuss the shear and vortex tilt because the vortex center above 400 hPa is hard to determine at times. Such concern was also discussed in Reasor et al. (2000) and Rogers et al. (2003). Because the inner-core shear directly influences the asymmetric distribution in the eyewall region (Braun et al. 2006), the shear in the inner-core region (150–300 km) is calculated to describe the response of the storm.

Hodographs of inner-core winds between 900 and 400 hPa demonstrate that at 0530 UTC 12 August (Fig. 8a), the inner-core shear is directed toward the west with a magnitude of $\sim$5.8 m s^{-1} between 900 and 650 hPa and it shifts to the northeast with a magnitude of $\sim$4.5 m s^{-1} between 650 and 400 hPa. The resulting 900–400-hPa shear is directed toward the north-northwest with a magnitude of $\sim$4.5 m s^{-1}. Two hours

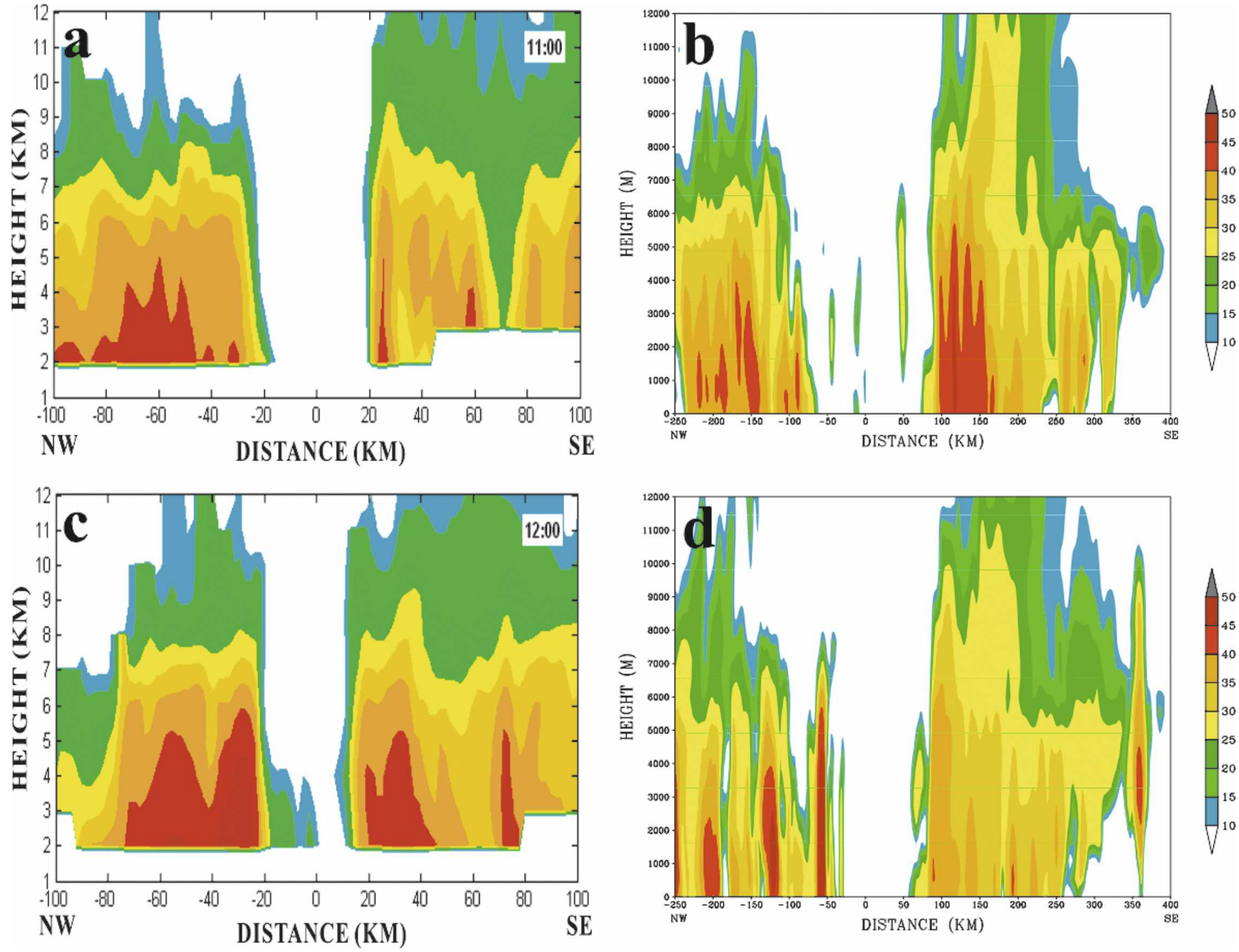

FIG. 7. Northwest–southeast vertical cross sections (along the arrow direction in Fig. 6c) of radar reflectivity (dBZ) observed in Wenzhou through the centers of the typhoon at (a) 1100 and (c) 1200 UTC 12 Aug. (b), (d) As in (a) and (c), respectively, but valid from the model results. Note that the horizontal scales are different between the model results and the radar observations.

later, the 900–650- and 650–400-hPa vertical shears still maintain a direction of west and northeast, respectively, and the 900–400-hPa shear points to the west-northwest with a magnitude of $\sim$4.5 m s^{-1} (Fig. 8b). Therefore the simulated inner-core vertical shear is not unidirectional vertically.

Consistent with the nonunidirectional wind shear, the direction of vortex tilt is not unidirectional with height. For example, the 900–650-hPa tilt is toward the west and the 650–400-hPa one leans toward the east at 0530 UTC 12 August (Fig. 9a). The vortex tilts generally downshear with height. Similar features can also be found at 0700 UTC 12 August (Fig. 9b). Similar to the findings by Rogers et al. (2003), the tilt magnitude is variable with many frequent pulses (Fig. 10). The tilt magnitude between 900 and 650 hPa ranges from about 4 to 23 km, accompanied by the inner-core vertical shear ranging from around 4 to 9 m s^{-1} (Fig. 10a). Before 0730 UTC 12 August, the magnitudes of both the 900–650-hPa tilt and shear tend to increase slightly. Half an hour later, the shear magnitude increases to $\sim$7.5 m s^{-1}, while the tilt drops abruptly to about 4 km. The reason why this sharp tilt change happens is not clear and needs to be investigated further. The vortex tilt between 900 and 650 hPa increases again after 0800 UTC 12 August when a sharp drop of the tilt magnitude occurs (Fig. 10a). This feature may be related to the penetration depth. Jones (1995) documented that vortex tilt also depends on penetration depth, which can be defined as $[f_{\rm loc}(f + \zeta)]^{1/2}L/N$, where $f_{\rm loc} = f + 2V_t/r$, f is the Coriolis parameter, V_t is the tangential wind, r is the radius, ζ is the vertical component of relative vorticity, L is the horizontal scale of the potential vorticity anomaly, and N is the Brunt–Väisälä frequency. Reducing the penetration depth gives rise to the vortex having a greater tilt. For the present case, after 0730

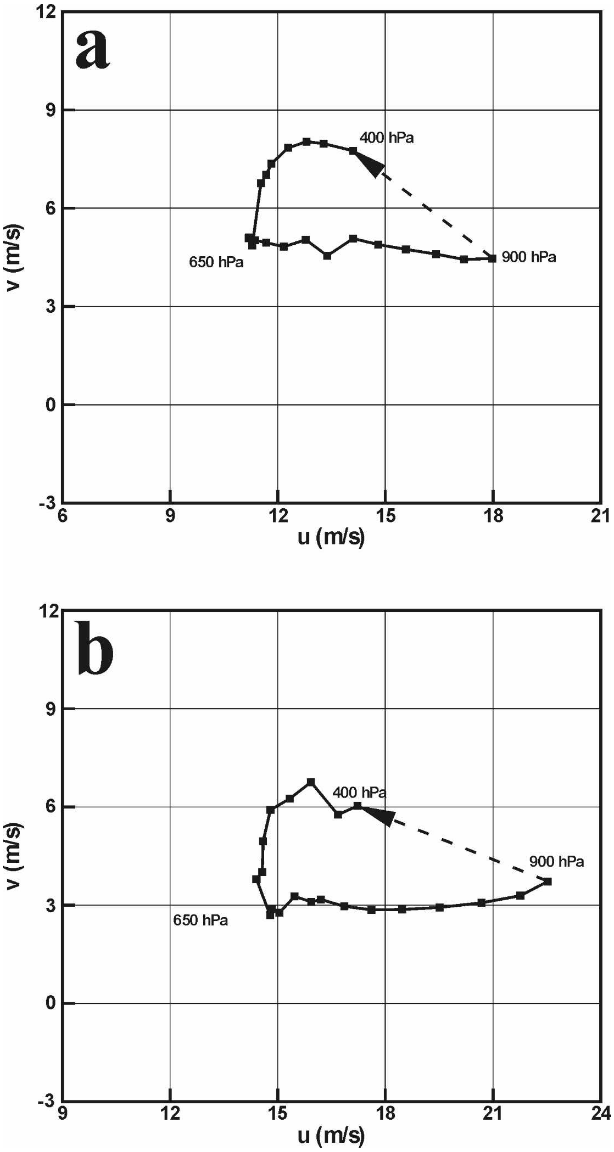

FIG. 8. Hodographs of inner-core winds between 900 and 400 hPa at (a) 0530 and (b) 0730 UTC 12 Aug. Arrows depict 900–400-hPa vertical shear vectors. Solid boxes show in turn wind values at 900, 875, 850, 825, 800, 775, 750, 725, 700, 675, 650, 625, 600, 575, 550, 525, 500, 475, 450, 425, and 400 hPa.

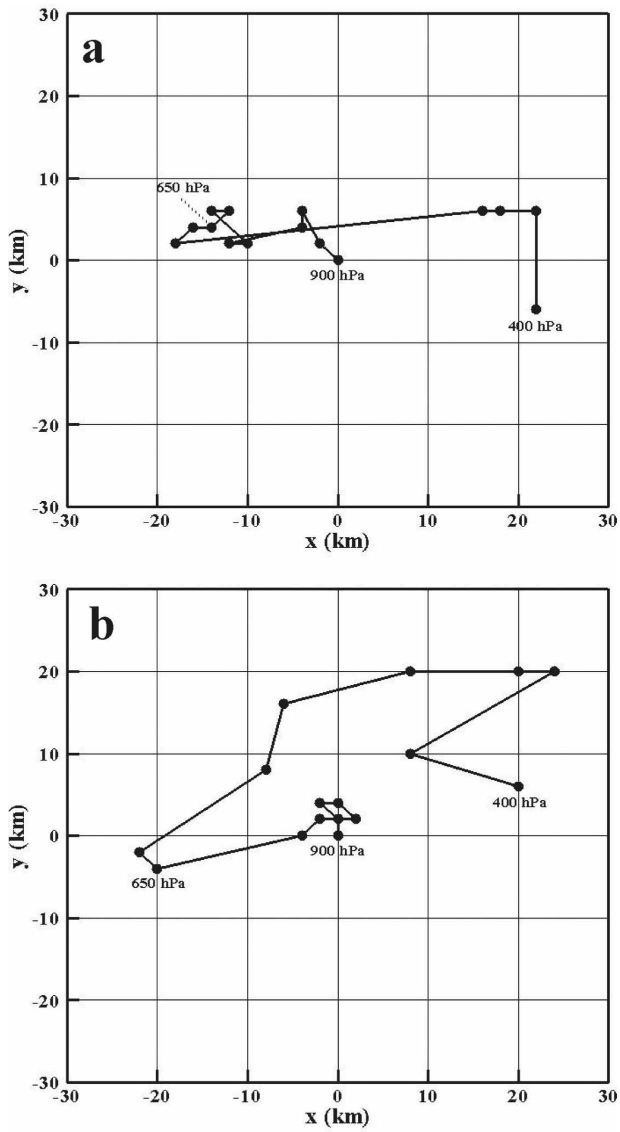

FIG. 9. Plots of displacement of vortex centers between 900 and 400 hPa relative to location of 900-hPa center at (a) 0530 and (b) 0730 UTC 12 Aug. Location of 900-hPa center is at (0, 0) location of chart.

UTC 12 August, part of the cold and dry inland air is advected toward the inner-core region at the lower–midlevels, which would lead to increased static stability (N becomes large) in the lower troposphere. Consequently, the penetration depth decreases and the vortex tilt increases (Fig. 10a). This mechanism is also documented by Wong and Chan (2004) in their MM5 simulations. The 900–650-hPa shear direction also changes from west-northwestward to westward during the 6-h period (Fig. 11) and the change in vortex tilt direction generally has the similar evolving trend except for the larger amplitude of the pulses.

The vortex tilt between 650 and 400 hPa ranges from ~6 to ~55 km and the corresponding inner-core shear magnitude ranges from ~1.0 to ~4.5 m s^{-1} during the period of interest (Fig. 10b). By 0630 UTC 12 August, the shear stops increasing, accompanied by a sustained enhancement of the vortex tilt. The inner-core shear then tends to decrease with some frequent pulses. In contrast, the 650–400-hPa vortex tilt is large until around 0700 UTC 12 August, and then it decreases. Although such large magnitudes of the vortex tilt in the

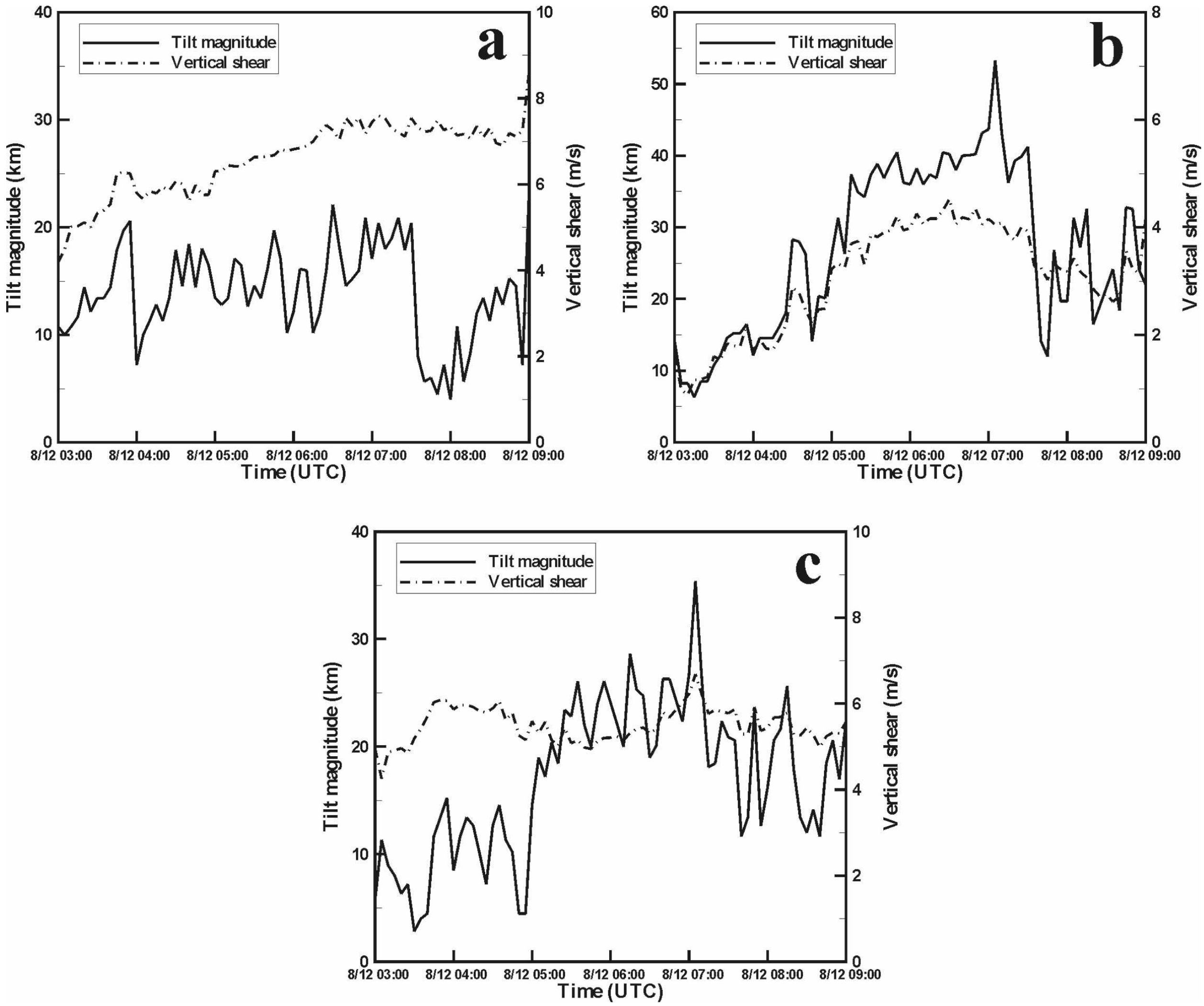

FIG. 10. Time series between 0300 and 0900 UTC 12 Aug of the magnitude of (a) the 900–650-, (b) 650–400-, and (c) 900–400-hPa wind shear (dashed–dotted lines; m s^{-1}) and tilt (solid lines; km). Tilt magnitude is calculated from the magnitude of the horizontal displacement of the upper storm center from the lower storm center, e.g., 650–400-hPa tilt magnitude from the horizontal displacement of the 400-hPa storm center from the 650-hPa storm center.

presence of weak shear are rarely found in previous simulations with moist models, the trends between the shear and vortex tilt demonstrate that such features of the vortex tilt are feasible. The direction of the shear between 650 and 400 hPa changes between eastward and north-northeastward and the corresponding vortex tilt direction changes between south-southeastward and north-northeastward (Fig. 11). The pulses in the directions of the 650–400-hPa shear and vortex tilt have similar variations. The evolution of the 900–400-hPa tilt magnitude appears not to correlate well with that of the shear (Fig. 10c). This shear is nearly constant with the magnitude of around 5.5 m s^{-1}, while the tilt shifts from smaller values prior to 0500 UTC August 12 to larger values thereafter. These results suggest that there may be two regimes: one where the shear is easterly between 900 and 650 hPa, and another where the shear is southwesterly between 650 and 400 hPa. The tilt and shear directions correlate well within each regime, but not across regimes.

The time-averaged fields of vertical velocity and precipitation mixing ratio for the period 0300–0730 UTC 12 August indicate that the maximum updrafts are just inside the region of maximum precipitation, and weak downdrafts are located primarily outside and downstream of the maxima of updrafts (Fig. 12). The lower-level maximum precipitation occurs in the southeastern portion of the eyewall (Fig. 12a). In addition, maximum upward motion exists upstream of the precipitation peak, which is similar to the results in Braun et al.

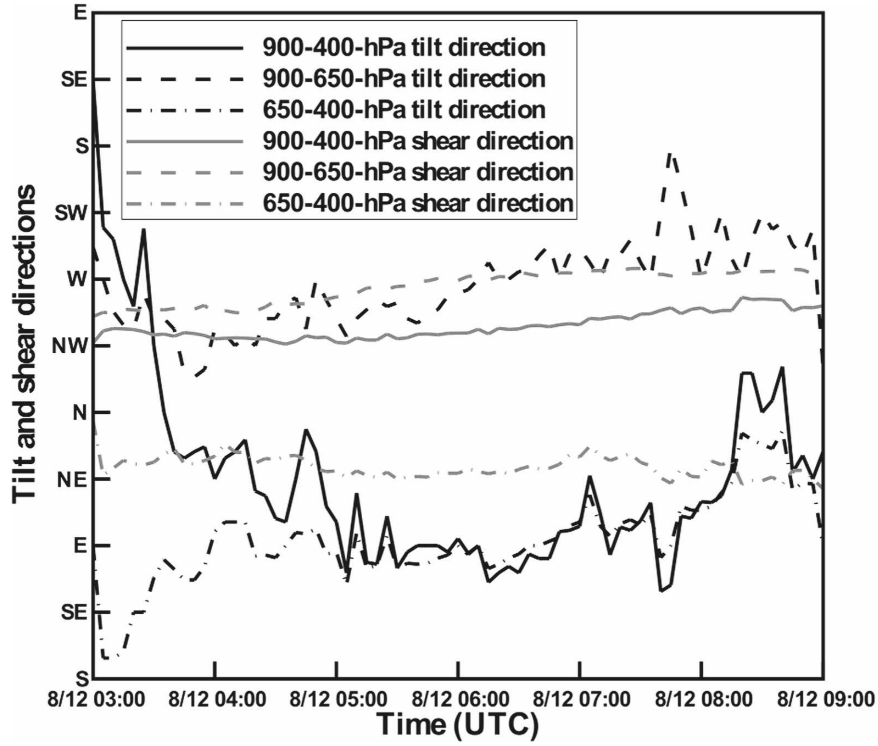

FIG. 11. As in Fig. 10, but for the 900–650-, 650–400-, and 900–400-hPa tilt direction (black lines) and shear direction (gray lines).

(2006). It is worth noting that the upward motion >0.4 m s^{-1} and mixing ratio >0.5 g kg^{-1} generally cover the main eyewall region except for the north, showing that the precipitation is concentrated on the left side of the averaged 900–650-hPa shear. It is indicated that the asymmetries in rainfall associated with the low-level shear and tilt have a greater impact at these altitudes, since that is generally the source layer for the convection and it is where the equivalent potential temperature is the highest. In contrast, the 525-hPa vertical motion and 500-hPa precipitation become significantly asymmetric, with the updrafts >0.4 m s^{-1} generally in the southeastern part of the eyewall (Fig. 12b). Similar to those at the lower level, the maximum updrafts and maximum precipitation lie on the southeastern side of the inner core, to the right of the 650–400-hPa shear. The 900–400-hPa shear vector is approximately perpendicular to the 900–400-hPa vortex tilt vector, and the strongest convection occurs on the rear side of the shear (Fig. 12c). These results thus are not representative of the downshear-left bias associated with a near unidirectional vertical shear from the lower levels to the upper levels in many numerical simulations (Frank and Ritchie 2001; Braun 2002; Braun et al. 2006; Wu et al. 2006).

As mentioned in the introduction, one mechanism for the relation between shear and convective asymmetry is the storm-relative asymmetric flow (Willoughby et al. 1984; Bender 1997; Braun et al. 2006; Wu et al. 2006). In the boundary layer, the relative flow is from the northwest to the southeast, which results in the region of lower-level convergence with the magnitude of about -4×10^{-4} s^{-1} in the northwestern portion of the eyewall (Fig. 13a). The vertical extent of the inflow in the northwestern portion is from the surface to the midtroposphere. In the eye region, strong asymmetric flow occurs at the midlevels (Fig. 13a). Such strong relative flow causes net convergence at the midlevels in the southeastern part of the eyewall. Inflow is also found above 550 hPa, so that the convergence extends at least up to 400 hPa (Fig. 13a). In the outflow layer above 400 hPa there is divergence (not shown), which is closely correlated with the previously mentioned large convergence in the southeastern part of the eyewall, contributing to the presence of the maximum upward motion and the most active convection in that region (see Fig. 12). In contrast, Fig. 13b shows a couplet of convergence and divergence located in the southwestern part of the eyewall. The storm-relative inflow is confined to the boundary layer in the southwest. The convergence forced by this inflow extends from the surface to near 700 hPa and spreads radially outward from 80 to 130 km from the center (Fig. 13b). The divergence–conver-

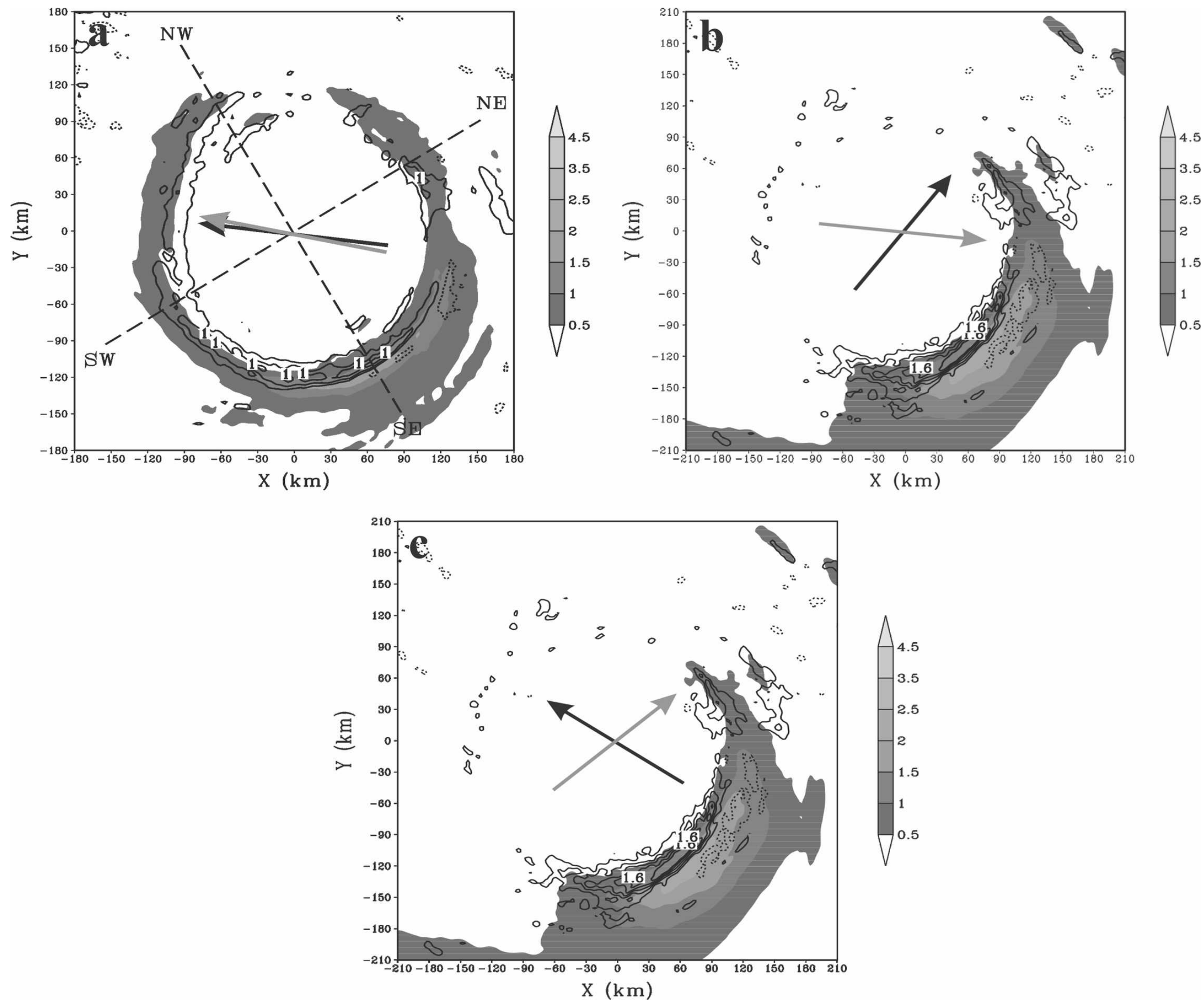

FIG. 12. Time-averaged total precipitation mixing ratio (shading; sum of rain and graupel) and vertical velocity (contours) for the period 0300–0730 UTC 12 Aug. Black and gray vectors indicate the direction of the near-core shear and vortex tilt, respectively. Vertical velocity contours are at intervals of 0.3 m s^{-1} for updrafts (solid lines) and 0.2 m s^{-1} for downdrafts (dashed lines). Zero value is neglected. Vertical velocity (mixing ratio) fields at (a) 750-hPa (725-hPa) level with the direction of vertical shear and vortex tilt between 900 and 650 hPa, (b) 525-hPa (500-hPa) level with the direction of vertical shear and vortex tilt between 650 and 400 hPa, and (c) 525-hPa (500-hPa) level with the direction of vertical shear and vortex tilt between 900 and 400 hPa. Dashed lines in (a) show the locations of radial cross sections in Fig. 13.

gence coupler is located at the inner edge of the convergence and extends from 875 to near 550 hPa. This divergence is likely associated with the sloped eyewall updraft as required by mass balance (Jorgensen 1984). In addition, relatively weak inflow occurs above 550 hPa in the southwest of the eyewall (Fig. 13b), which triggers the occurrence of weak convergence at the upper levels. These distributions of convergence and divergence associated with the storm-relative flow cause the updraft and convection to be concentrated beneath the midtroposphere in the southwestern part of the eyewall (Fig. 12).

The horizontal distributions of the storm-relative flow and divergence show that a convergence ring occupies the eyewall region in the boundary layer (Fig. 14a). The relative flow represents a wavenumber-1 asymmetry with the inflow in the western quadrant and the outflow in the eastern quadrant. The outflow in the east results in the divergence dominant outside the eyewall. At 875 hPa, there is a ringlike divergence that is associated with the sloped eyewall updraft located at the inner edge of the lower-level eyewall, accompanied with a convergent ring just outside of it (Fig. 14b). Divergent areas can be observed further out to the east.

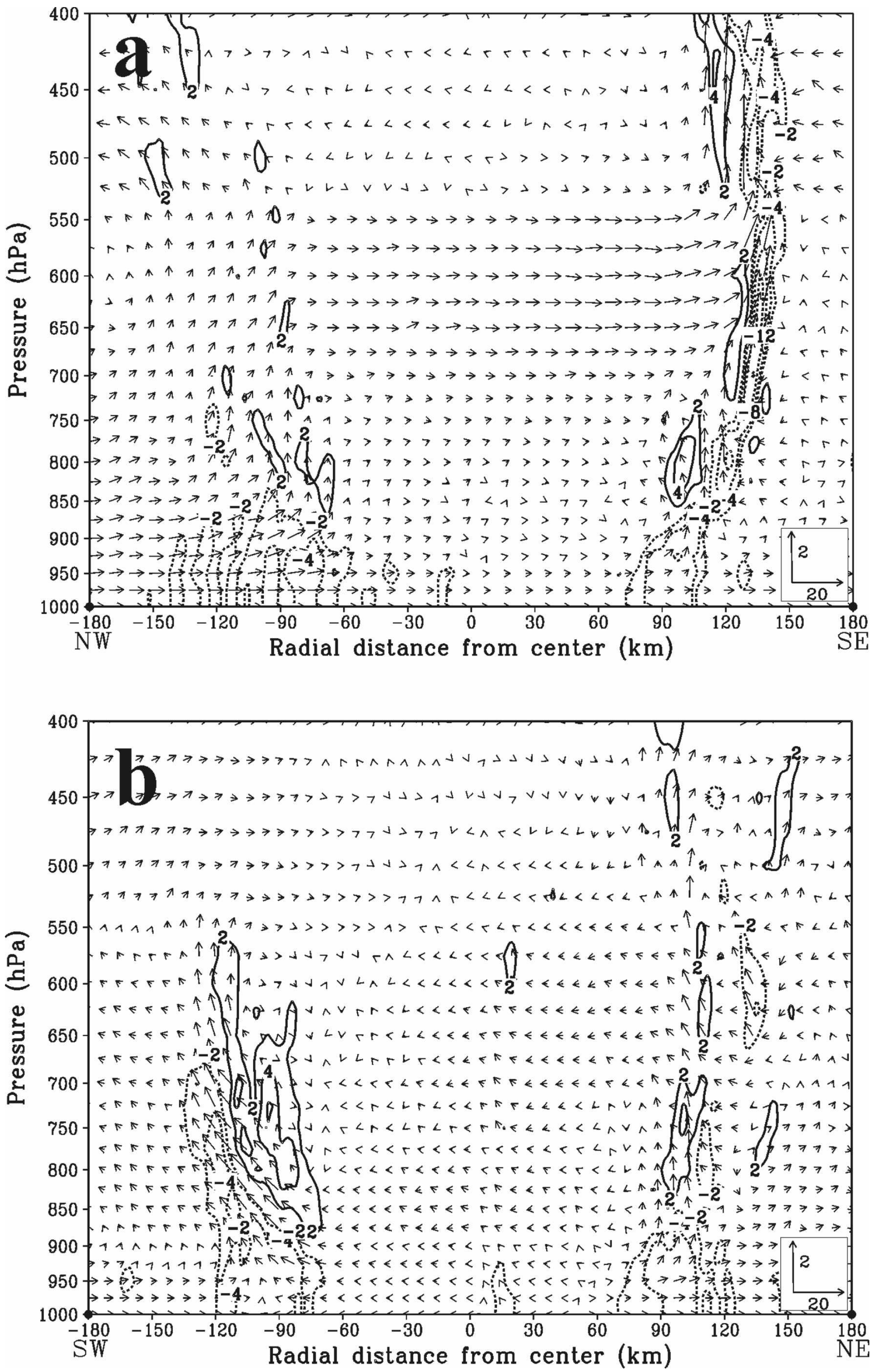

FIG. 13. Vertical cross sections through the typhoon center and in the (a) northwest–southeast and (b) southwest–northeast directions of the time-averaged asymmetric relative wind-vertical flow field (arrows) and the horizontal divergence (contours; 10^{-4} s^{-1}).

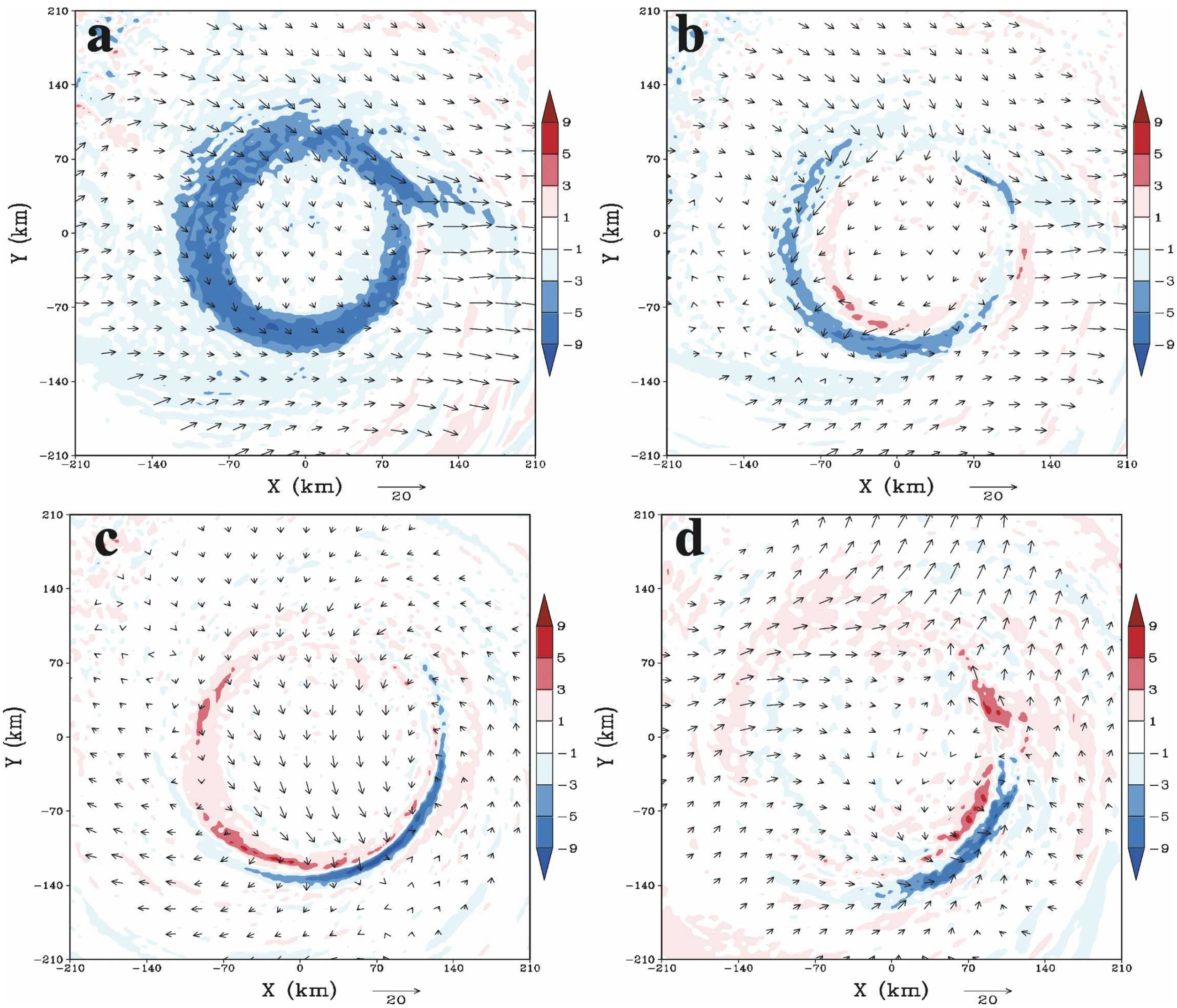

FIG. 14. Time-averaged (a) 950-, (b) 875-, (c) 650-, and (d) 400-hPa divergence (shading; 10^{-4} s^{-1}) and asymmetric winds (vectors).

The storm-relative flow at 875 hPa is characterized by two major flows, one approaching from the northwest, the other from the southwest, impinging on the northern and southern sides, respectively, and continuing eastward on the eastern side. Interestingly, the 950- and 875-hPa asymmetric flows within the eye are weak and seemingly unconnected to the storm-relative flows. This feature suggests that the eyewall behaves like a containment vessel which can inhibit ventilation of the eye by the outer mean flow (McWilliams 1984; McIntyre 1993; Willoughby 1998; Braun et al. 2006).

The divergence is predominant in the southwestern and western parts of the eyewall, and the net convergence is located in the southeast at 650 hPa (Fig. 14c). As shown in Fig. 13a, the strong asymmetric winds exist at 650 hPa within the eye, which is speculated on being associated with the nonunidirectional vortex tilt. The downward projection of the upper potential-vorticity anomaly approximately to the east of the midlevel anomaly gives a cyclonic circulation in the midlayer. This flow has a northerly component across the center of the anomaly. The similarity occurs for the lower anomaly also lying east of the midlevel anomaly, which imposes another northerly component across the center of the midlevel anomaly through its upward projection. These northerly components jointly strengthen the asymmetric flow within the center region at the midlevel. The analysis of potential vorticity inversion might be an ideal way to confirm this speculative cause for the presence of the strong asymmetric flow inside the eye region, but it is out of the scope in the current study. In 400-hPa layer, the strong storm-relative outflow dominates the north of the storm, resulting in the large areas with divergence there (Fig. 14d). An inflow approaches

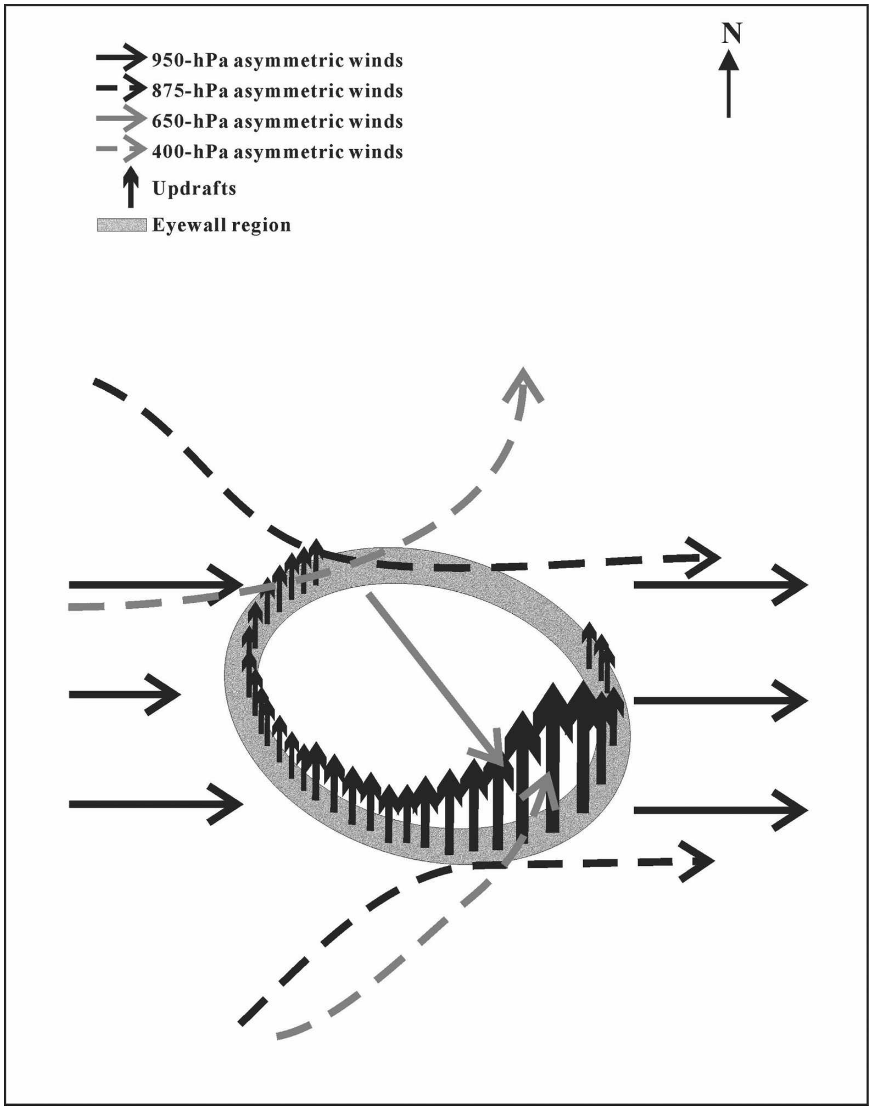

FIG. 15. Schematic diagram illustrating the storm-relative asymmetric flow pattern associated with Typhoon Rananim.

the southeast of the eyewall and brings the net convergence generating there.

As summarized in Fig. 15, the westerly asymmetric inflows in the boundary layer (black solid arrows) and the northwesterly and southerly inflows in the lower troposphere (black dashed arrows) cause convergence covering the majority of the eyewall region. The collocation between the inflow-induced lower-level convergence and midlevel divergence results in shallow updrafts in the west and south of the eyewall. A strong northwesterly asymmetric flow inside the eye region at the midlevel (gray solid arrow) and the southwesterly inflows near 400 hPa (gray dashed arrow) produce net convergence in the southeast of the eyewall, which results in the maxima of the upward motion in the southeastern portion of the eyewall by coupling with the divergence above 400 hPa. These features are in accordance with the vorticity balance argument in Bender (1997), which states that the direction of the storm-relative flow controls the location of the precipitation peaks.

5. Summary

In this paper the MM5 model is employed to simulate the development and evolution of Typhoon Rananim (2004) from 0000 UTC 10 August to 0000 UTC 13 August with the finest grid size of 2 km to resolve the inner core of the typhoon. The model is initialized with the NCEP analysis and with incorporation of a model-generated vortex. It successfully reproduces the storm path and intensity change as verified against the best-track data. Except for the period of initial model adjustment, the simulated track is close to the best track, with the landfall location and time nearly coinciding with the observed. The observed and the simulated intensities during the 72-h period compare fairly well, including the steady deepening in the first 36 h of integration, its subsequent maintenance, and its weakening after landfall. Nevertheless, the simulated peak intensity is about 6 hPa higher than the observed. Compared with the radar observation near landfall, the model also reproduces well the asymmetry of the deep convection in the inner-core region and eyewall tilt, although the model produces a much bigger eye than the observed one and does not capture some features associated with the inner rainbands. The model captures the asymmetric features of surface winds, reproduces especially well the distribution of surface winds in the inner core of the storm. Changes in wind speed and direction and surface pressure near the storm center during landfall are reproduced also fairly well by the model in comparison with the available observations.

To investigate how vertical shear impacts on the asymmetric convection in the inner-core region, the shear-induced vortex tilt and storm-relative asymmetric winds are examined in this study. It is indicated that the inner-core vertical shear of Rananim is nonunidirectional vertically during its mature stage, with the time-averaged inner-core shear between 900 and 650 hPa from east-southeast and the shear between 650 and 400 hPa from southwest. Such a nonunidirectional shear results in a nonunidirectional vortex tilt. The time-averaged vertical motion in the lower layer is slightly asymmetric with updrafts located in the southern semicircle and northwest of the eyewall, and the vertical motion in the midtroposphere is significantly asymmetric with the maxima of updrafts in the southeastern eyewall. These distributions of asymmetric convection are inconsistent with the typical downshear-left pattern for a deep-layer shear, but can be explained well by the vorticity balance argument (e.g., Bender 1997). In the Rananim simulation, the collocation between the inflow-induced convergence in the boundary layer and in the lower troposphere and divergence at the midlevels results in shallow updrafts in the western semicircle and southern part of the eyewall. The convective maxima in the southeastern eyewall are qualitatively related to the corresponding collocation between the net convergence associated with the strong asymmetric flow in the midtroposphere and the inflow near 400 hPa and the divergence in the outflow layer above 400 hPa.

In this paper, we have focused on the verification of the simulation of Typhoon Rananim and the inner-core convective asymmetry corresponding to the inner-core vertical shear, vortex tilt, and storm-relative flow. Nonunidirectional inner-core shear causing nonunidirectional vortex tilt is found, which cause the asymmetric convection to be inconsistent with the typical downshear-left pattern for a deep-layer shear. This finding indicates the complexity of the convection in a TC, and provides challenges for the prediction of the precipitation associated with a TC, especially near landfall. Only paying attention to the relation between the deep-layer shear and the asymmetric convection may cause incorrect forecasting of TC precipitation and wind.

Based on the results of this high-resolution simulation, further diagnostic analyses are under way to examine the kinematics and dynamics of the simulated storm. In particular, special attention is being given to inner-core dynamics, including the activity of vortex Rossby waves, and mesovortices in the eyewall as the storm is affected by the coastline and topography. Relevant results will be given in subsequent publications.

Acknowledgments. This work was supported in part by the National Natural Science Foundation of China under Grants 40575030, 40333025, 40505004, and 40675060; the Ministry of Science and Technology of China under Grants 2005DIB3J104 and 2006AA09Z151; the Chinese State Oceanic Administration project 908-02-03-10; and the open project of the Laboratory of Physical Oceanography, Ocean University of China. We are grateful to Dr. Yuqing Wang, Prof. Johnny C. L. Chan, Dr. Baode Chen, and Ms. Wen Mi for providing constructive comments, and to Dr. Kun Zhao for furnishing the observational radar imagery. The authors express their gratitude to two anonymous reviewers whose comments helped to improve the manuscript.

REFERENCES

Bender, M. A., 1997: The effect of relative flow on the asymmetric structure in the interior of hurricanes. *J. Atmos. Sci.,* **54,** 703–724.

Betts, A. K., and M. J. Miller, 1986: A new convective adjustment scheme. Part II: Single column tests using GATE wave, BOMEX, ATEX and Arctic air-mass data set. *Quart. J. Roy. Meteor. Soc.,* **112,** 693–709.

Black, M. L., J. F. Gamache, F. D. Marks Jr., C. E. Samsury, and H. E. Willoughby, 2002: Eastern Pacific Hurricanes Jimena of 1991 and Olivia of 1994: The effect of vertical shear on structure and intensity. *Mon. Wea. Rev.,* **130,** 2291–2312.

Braun, S. A., 2002: A cloud-resolving simulation of Hurricane Bob (1991): Storm structure and eyewall buoyancy. *Mon. Wea. Rev.,* **130,** 1573–1592.

——, and W.-K. Tao, 2000: Sensitivity of high-resolution simulations of Hurricane Bob (1991) to planetary boundary layer parameterizations. *Mon. Wea. Rev.,* **128,** 3941–3961.

——, M. T. Montgomery, and Z. Pu, 2006: High-resolution simulation of Hurricane Bonnie (1998). Part I: The organization of eyewall vertical motion. *J. Atmos. Sci.,* **63,** 19–42.

Chan, J. C. L., 1984: An observational study of the physical processes responsible for tropical cyclone motion. *J. Atmos. Sci.,* **41,** 1036–1048.

——, Y. Duan, and L. K. Shay, 2001: Tropical cyclone intensity change from a Simple ocean–atmosphere coupled model. *J. Atmos. Sci.,* **58,** 154–172.

——, F. M. F. Ko, and Y. M. Lei, 2002: Relationship between potential vorticity tendency and tropical cyclone motion. *J. Atmos. Sci.,* **59,** 1317–1336.

——, K. S. Liu, S. E. Ching, and E. S. T. Lai, 2004: Asymmetric distribution of convection associated with tropical cyclones making landfall along the south China coast. *Mon. Wea. Rev.,* **132,** 2410–2420.

Davis, C. A., and L. F. Bosart, 2001: Numerical simulations of the genesis of Hurricane Diana (1984). Part I: Control simulation. *Mon. Wea. Rev.,* **129,** 1859–1881.

DeMaria, M., and J. Kaplan, 1997: An operational evaluation of a statistical hurricane intensity prediction scheme (SHIPS). Preprints, *22nd Conf. on Hurricanes and Tropical Meteorology,* Fort Collins, CO, Amer. Meteor. Soc., 280–281.

Dudhia, J., 1989: Numerical study of convection observed during the Winter Monsoon Experiment using a mesoscale two-dimensional model. *J. Atmos. Sci.,* **46,** 3077–3107.

——, 1993: A nonhydrostatic version of the Penn State–NCAR Mesoscale Model: Validation tests and simulation of an Atlantic cyclone and cold front. *Mon. Wea. Rev.,* **121,** 1493–1513.

Frank, W. M., and E. A. Ritchie, 1999: Effects of environmental flow upon tropical cyclone structure. *Mon. Wea. Rev.,* **127,** 2044–2061.

——, and ——, 2001: Effects of vertical wind shear on the intensity and structure of numerically simulated hurricanes. *Mon. Wea. Rev.,* **129,** 2249–2269.

Franklin, J. L., S. J. Lord, S. E. Feuer, and F. D. Marks Jr., 1993: The kinematic structure of Hurricane Gloria (1985) determined from nested analyses of dropwindsonde and Doppler radar data. *Mon. Wea. Rev.,* **121,** 2433–2451.

George, J. E., and W. M. Gray, 1976: Tropical cyclone motion and surrounding parameter relationships. *J. Appl. Meteor.,* **15,** 1252–1264.

Grell, G. A., J. Dudhia, and D. R. Stauffer, 1995: A description of the fifth-generation Penn State–NCAR Mesoscale Model (MM5). NCAR Tech. Note NCAR/TN-398+STR, 122 pp.

Holland, G. J., 1983: Tropical cyclone motion: Environmental interaction plus a beta effect. *J. Atmos. Sci.,* **40,** 328–342.

——, 1984: Tropical cyclone motion: A comparison of theory and observation. *J. Atmos. Sci.,* **41,** 68–75.

Ian, M., S. Businger, F. Marks, P. Dodge, and J. A. Businger, 2005: An observational case for the prevalence of roll vortices in the hurricane boundary layer. *J. Atmos. Sci.,* **62,** 2662–2673.

Jones, S. C., 1995: The evolution of vortices in vertical shear. I: Initially barotropic vortices. *Quart. J. Roy. Meteor. Soc.,* **121,** 821–851.

Jorgensen, D. P., 1984: Mesoscale and convective-scale characteristics of mature hurricanes. Part II: Inner core structure of Hurricane Allen (1980). *J. Atmos. Sci.,* **41,** 1287–1311.

Kurihara, Y., M. A. Bender, R. E. Tuleya, and R. J. Ross, 1995: Improvements in the GFDL hurricane prediction system. *Mon. Wea. Rev.,* **123,** 2791–2801.

Kwon, H. J., S.-H. Won, M.-H. Ahn, A.-S. Suh, and H.-S. Chung, 2002: GFDL-type typhoon initialization in MM5. *Mon. Wea. Rev.,* **130,** 2966–2974.

Liu, Y., D.-L. Zhang, and M. K. Yau, 1997: A multiscale numerical study of Hurricane Andrew (1992). Part I: Explicit simulation and verification. *Mon. Wea. Rev.,* **125,** 3073–3093.

——, ——, and ——, 1999: A multiscale numerical study of Hurricane Andrew (1992). Part II: Kinematics and inner core structures. *Mon. Wea. Rev.,* **127,** 2597–2616.

Marks, F. D., R. A. Houze, and J. F. Gamache, 1992: Dual-aircraft investigation of the inner core of Hurricane Norbert. Part I: Kinematic structure. *J. Atmos. Sci.,* **49,** 919–942.

McIntyre, M. E., 1993: Isentropic distributions of potential vorticity and their relevance to tropical cyclone dynamics. *Tropical Cyclone Disaster: Proceedings of ISCU/WMO International Symposium,* Z. Zheng, G. Holland, and L. Emanuel, Eds., Peking University Press, 143–156.

McWilliams, J. C., 1984: The emergence of isolated coherent vortices in turbulent flow. *J. Fluid Mech.,* **146,** 21–43.

Montgomery, M. T., and R. J. Kallenbach, 1997: A theory for vortex Rossby-waves and its application to spiral bands and intensity changes in hurricanes. *Quart. J. Roy. Meteor. Soc.,* **123,** 435–465.

Neumann, C. J., 1997: National plan for tropical cyclone research. FCM Rep. FCM-P_{25}-1997, 100 pp.

Powell, M. D., and S. H. Houston, 1998: Surface wind fields of 1995 Hurricanes Erin, Opal, Luis, Marilyn, and Roxanne at landfall. *Mon. Wea. Rev.,* **126,** 1259–1273.

Reasor, P. D., M. T. Montgomery, F. D. Marks Jr., and J. F. Gamache, 2000: Low-wavenumber structure and evolution of the hurricane inner core observed by airborne dual-Doppler radar. *Mon. Wea. Rev.,* **128,** 1653–1680.

Reisner, J., and R. T. Bruintjes, 1998: Explicit forecasting of supercooled liquid water in winter storms using the MM5 mesoscale model. *Quart. J. Roy. Meteor. Soc.,* **124,** 1071–1107.

Rogers, R., S. Chen, J. Tenerelli, and H. Willoughby, 2003: A numerical study of the impact of vertical shear on the distribution of rainfall in Hurricane Bonnie (1998). *Mon. Wea. Rev.,* **131,** 1577–1599.

Soden, B. J., C. S. Velden, and R. E. Tuleya, 2001: The impact of satellite winds on experimental GFDL hurricane model forecasts. *Mon. Wea. Rev.,* **129,** 835–852.

Tuleya, R. E., and S. J. Lord, 1997: The impact of dropwindsonde data on GFDL hurricane model forecasts using global analyses. *Wea. Forecasting,* **12,** 307–323.

Wang, B., R. L. Elsberry, Y. Wang, and L. Wu, 1998: Dynamics in tropical cyclone motion: A review. *Chin. J. Atmos. Sci.,* **22,** 535–547.

Wang, Y., 2002a: Vortex Rossby waves in a numerically simulated tropical cyclone. Part I: Overall structure, potential vorticity, and kinetic energy budgets. *J. Atmos. Sci.,* **59,** 1213–1238.

——, 2002b: Vortex Rossby waves in a numerically simulated tropical cyclone. Part II: The role in tropical cyclone structure and intensity changes. *J. Atmos. Sci.,* **59,** 1239–1262.

——, and C.-C. Wu, 2004: Current understanding of tropical cyclone structure and intensity changes—A review. *Meteor. Atmos. Phys.,* **87,** 257–278.

——, and G. J. Holland, 1996: The beta drift of baroclinic vortices. Part I: Adiabatic vortices. *J. Atmos. Sci.,* **53,** 411–427.

Willoughby, H. E., 1998: Tropical cyclone eye thermodynamics. *Mon. Wea. Rev.,* **126,** 3053–3067.

——, F. D. Marks Jr., and R. J. Feinberg, 1984: Stationary and moving convective bands in hurricanes. *J. Atmos. Sci.,* **41,** 3189–3211.

Wong, M. L. M., and J. C. L. Chan, 2004: Tropical cyclone intensity in vertical wind shear. *J. Atmos. Sci.,* **61,** 1859–1876.

Wu, L., and B. Wang, 2001: Effects of convective heating on movement and vertical coupling of tropical cyclones: A numerical study. *J. Atmos. Sci.,* **58,** 3639–3649.

——, ——, and S. A. Braun, 2005: Impacts of air–sea interaction on tropical cyclone track and intensity. *Mon. Wea. Rev.,* **133,** 3299–3314.

——, S. A. Braun, J. Halverson, and G. Heymsfield, 2006: A numerical study of Hurricane Erin (2001). Part I: Model verification and storm evolution. *J. Atmos. Sci.,* **63,** 65–86.

Yau, M. K., Y. Liu, D.-L. Zhang, and Y. Chen, 2004: A multiscale numerical study of Hurricane Andrew (1992). Part VI: Small-scale inner-core structures and wind streaks. *Mon. Wea. Rev.,* **132,** 1410–1433.

Zhang, D.-L., and R. A. Anthes, 1982: A high-resolution model of the planetary boundary layer—sensitivity tests and comparisons with SESAME-79 data. *J. Appl. Meteor.,* **21,** 1594–1609.

——, Y. Liu, and M. K. Yau, 2000: A multiscale numerical study of Hurricane Andrew (1992). Part III: Dynamically induced vertical motion. *Mon. Wea. Rev.,* **128,** 3772–3788.

——, ——, and ——, 2001: A multiscale numerical study of Hurricane Andrew (1992). Part IV: Unbalanced flows. *Mon. Wea. Rev.,* **129,** 92–107.

——, ——, and ——, 2002: A multiscale numerical study of Hurricane Andrew (1992). Part V: Inner-core thermodynamics. *Mon. Wea. Rev.,* **130,** 2745–2763.

Zhang, Q.-H., S.-J. Chen, Y.-H. Kuo, K.-H. Lau, and R. A. Anthes, 2005: Numerical study of a typhoon with a large eye: Model simulation and verification. *Mon. Wea. Rev.,* **133,** 725–742.

Zhu, T., and D.-L. Zhang, 2006: Numerical simulation of Hurricane Bonnie (1998). Part II: Sensitivity to varying cloud microphysical processes. *J. Atmos. Sci.,* **63,** 109–126.

——, ——, and F. Weng, 2004: Numerical simulation of Hurricane Bonnie (1998). Part I: Eyewall evolution and intensity changes. *Mon. Wea. Rev.,* **132,** 225–241.